Application of Bi-State Magnetic Material to an Automotive IPM Starter/Alternator Machine

Ayman M. EL-Refaie, *Student Member, IEEE,* and Thomas M. Jahns, *Fellow, IEEE*

***Abstract*—A new bi-state soft magnetic material has been developed that can have its normally high magnetic permeability reduced permanently to that of air by means of heat treatment. As a result, localized heating via laser or other means can be used to locally "unmagnetize" regions in machine laminations while retaining the high permeability of adjacent untreated regions. A 6 kW interior permanent magnet (IPM) direct-drive starter/alternator machine was used as the target for this investigation. Two alternative designs for the same set of starter/alternator specifications are presented using the new magnetic material for the rotor laminations. Lumped-parameter magnetic circuit models including saturation were used to design both machines and the electromagnetic performance results were subsequently confirmed using finite element analysis (FEA). These results indicate that the performance specifications can be met using this new material while significantly increasing the mechanical integrity of the rotor at high speeds. Advantages and limitations of using this new bi-state magnetic material in IPM machine designs for starter/alternators and other applications are discussed.**

***Index Terms*—Magnetic materials, permanent magnet machines, rotating machine mechanical factors, synchronous machines.**

I. Introduction

A NEW bi-state soft magnetic material has recently been developed [1] that offers the intriguing property of adjustable permeability by means of heat treatment. That is, sufficient heating of this material causes its relative permeability to permanently drop by nearly three orders of magnitude from approximately 900 to 1 (i.e., air). Since this heating can be achieved locally within a given sample, the material provides the basis for designing monolithic soft magnetic structures consisting of adjacent regions of high and low permeability (Fig. 1) without the need for welding or joining of magnetic and nonmagnetic materials.

Table I provides a tabulation of key magnetic and mechanical properties for this new material (designated YEP-FA1 by its manufacturer) in the two right-most columns. The tradeoff between magnetic permeability and mechanical strength is apparent by comparing these two columns for the material with (Mag.) and without (Nonmag.) heat treatment. While heat treatment reduces the permeability by 900:1, the mechanical yield stress suffers to a much lesser degree, dropping by a factor of less than two from 640 MPa to 350 MPa. Even in its heat-treated condition, the material's yield stress is as high as that of conventional magnetic silicon steels such as M19 (350 MPa).

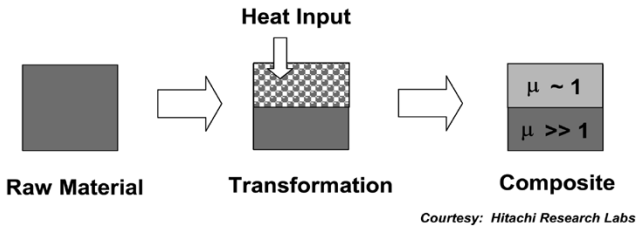

Fig. 1. Concept of new bi-state soft magnetic material.

TABLE I
COMPARISON OF KEY PROPERTIES OF THE YEP-FA1 BI-STATE SOFT MAGNETIC MATERIAL AND M19

	M19	YEP-FA1	
Composite	Si-Fe	Fe-17.5Cr-0.5C	
Magnetic Process	-	Heat Treatment	
Magnetic Properties	Magnetic	Magnetic	Nonmag
Permeability	8000	900	≤1.01
Coercive Force[KA/m]	0.038	0.5	-
Saturation Flux Density [T]	1.9	1.3	-
Mechanical Properties			
Yield Stress [MPa]	320-350	640	350
UTS [MPa]	503	770	930
Elongation [%]	23	15	40
Hardness [Hv]	151	220	220

These characteristics are appealing for a variety of machine and actuator applications [2]–[4]. For example, they open opportunities for designing rotor laminations for interior permanent magnet (IPM) synchronous machines that escape one of the greatest engineering dilemmas associated with the use of conventional silicon steel laminations [5]. That is, much wider steel bridges can be introduced at the ends and mid-points of the rotor magnet cavities that significantly improve the mechanical integrity of the rotor without the accompanying disadvantages of low-reluctance shunting paths between the magnet north and south poles. (See Fig. 5 for graphical identification of the bridges and center posts.) This offers a significant new degree of freedom in the design of future IPM machines.

Additional tradeoffs are also apparent in Table I. In exchange for the bi-state magnetic characteristics, the new material offers lower saturated flux density and higher coercive force values than conventional silicon steels. Furthermore, the cost of this new material in the stainless steel family is expected to be higher than silicon steel.

The purpose of this paper is to explore the benefits and limitations of this new bi-state magnetic material when applied

Manuscript received April 16, 2003; revised August 25, 2003. This work was supported by the MIT/Industry Consortium on Advanced Automotive Electrical/Electronic Components and Systems. Paper no. TEC-00093-2003.

The authors are with the University of Wisconsin–Madison, Madison, WI 53706 USA (e-mail: elrefaie@cae.wisc.edu).

Digital Object Identifier 10.1109/TEC.2004.841512

to a specific IPM machine application. In particular, a direct-drive automotive starter-alternator (S/A) application that has previously been addressed using conventional M19-grade silicon steel [6] was selected in order to provide a convenient basis for direct comparisons. An identical set of performance specifications was used for this new design exercise, including 150 N-m starting torque and 6 kW power generation at 6000 rpm.

Performance comparisons are provided using a variety of criteria including volume, size, weight, cost, and peak rotor mechanical stress. Although specific to this machine, such comparisons are useful for providing guidance on how this material can be applied most effectively to other applications.

II. Machine Design Approach

The design tool used for this investigation is the same one used previously to design the starter/alternator machine using conventional silicon steel for both the stator and rotor [6]. More specifically, this design software combines a nonlinear lumped-parameter magnetic circuit model of the IPM machine with a Monte Carlo optimization algorithm in order to find the best machine design to minimize cost. The magnetic lumped-parameter model developed to analyze the IPM machine includes magnetic saturation that particularly affects the rotor iron permeances along the q-axis, orthogonal to the magnet field orientation [7].

Electromagnetic finite element analysis has also been used for the final machine designs in order to verify key electrical parameters and to evaluate their torque ripple characteristics. A lumped-parameter thermal model is also incorporated into the software to evaluate all of the key steady-state temperatures within each candidate machine design [8].

Early in the investigation it became clear that attention should be focused on designs that use silicon steel such as M19 for the stator laminations and bi-state magnetic material for the rotor laminations only. Attempts to use the bi-state magnetic material for both the stator and the rotor resulted in unacceptably poor machine characteristics because of the lower permeability and saturation flux density of the composite material compared to M19 silicon steel. Since the properties of the YEP-FA1 material are only particularly needed for the IPM rotor bridges and center posts, it makes sense to apply it only in the rotor while retaining conventional silicon steel for the stator.

An initial investigation was made to calculate machine performance when all of the dimensions of the original S/A machine are retained so that the only change is to replace the rotor M19 steel with the YEP-FA1 bi-state material. It was quickly confirmed that this approach leads to unacceptable machine performance because of the poorer magnetic properties of the YEP-FA1 material compared to those of M19. It became clear that any success with the bi-state material must permit the machine dimensions to be optimized for this new material within the fixed maximum constraint on outer machine diameter (300 mm).

Two alternative design approaches using the YEP-FA1 material have been investigated during this study. The first design approach (Design #1) assumes that both the bridges at the ends of the rotor magnet cavities and the center posts at their midpoints are heat-treated so that they are nonmagnetic (i.e., $\mu = 1$). The second approach (Design #2) assumes that only the center posts are nonmagnetic; thin saturable bridges are retained at the ends of the cavities.

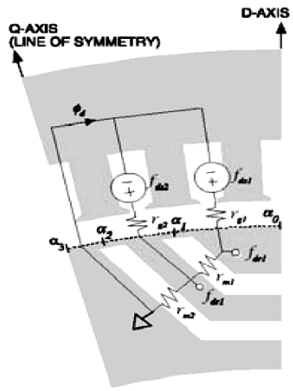

Fig. 2. Magnetic equivalent circuit for calculating L_d.

For both cases, the lumped-parameter magnetic circuit models for calculating the stator inductances and the magnet flux linkage have been modified appropriately to include the new regions of nonmagnetic material. An overview of these lumped-parameter models using conventional steel and the modifications needed to represent the introduction of the new bi-state magnetic material will be presented in the following subsections.

A. Stator d-Axis Inductance (L_d) Calculations

Fig. 2 shows the magnetic equivalent circuit for calculating the stator d-axis inductance L_d for the baseline case of M19 steel. Note that the d-axis is defined to be aligned with the magnet flux as shown in Fig. 2. A key assumption is made that the bridges and center posts are fully saturated by the magnet flux. As a result, the incremental permeability of the bridges and posts is assumed to be the same as that of air ($\mu = 1$).

For each of the two magnet layers, the lumped reluctance of the magnet should actually appear in parallel with the saturated bridge and center post reluctances to provide a detailed representation of the magnetic circuit. Since the bridges and posts are very narrow compared to the widths of the magnets, the saturated reluctances of these elements are very high compared to that of magnet layer. As a result, their effect on the parallel combined reluctance is negligible, and the total reluctance can be modeled as that of the magnet alone, as shown in Fig. 2. Subsequent electromagnetic analysis has supported the validity of this approach, confirming that the reluctances of the bridges and center posts are sufficiently high that they have almost no shunting effect on the magnet flux.

In the case of the new bi-state magnetic material, the bridges are assumed to be nonmagnetic (i.e., $\mu = 1$). Since this is the same assumption that was made for the saturated bridges and center posts in the original design as described above, no modification of the original d-axis model in Fig. 2 is required for either Design #1 or Design #2.

It should be noted that subsequent testing of a prototype version of the original starter/alternator machine using all M19

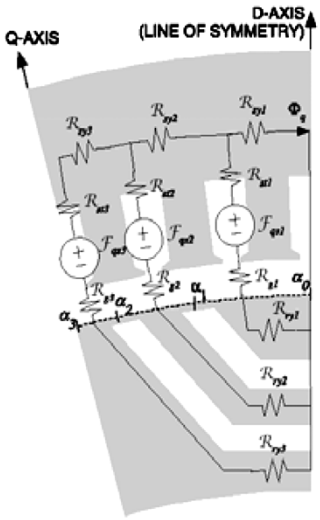

Fig. 3. Magnetic equivalent circuit for calculating L_q.

steel has shown that the bridges and center posts are not fully saturated under light-load conditions [9]. This creates some error between the value of L_d predicted by the lumped-parameter model and the actual measured value when the d-axis current is close to zero. This same observation applies to Design #2 that retains the saturating bridges, leading to some error in the light-load L_d prediction that will be discussed later in Section III.B of this paper when the results of finite element analysis are presented.

B. Stator q-Axis Inductance (L_q) Calculations

Fig. 3 shows the magnetic equivalent circuit that is used for calculating the stator q-axis inductance L_q for all three machine design cases. Each of the three rotor reluctances, R_{ry1}, R_{ry2}, and R_{ry3}, is formulated to include the effects of magnetic saturation. When the bi-state magnetic material is used for the rotor, the same basic equivalent circuit can be applied as for the baseline case of M19 material.

However, the outer bridges along the rotor surface have a similar electromagnetic effect as slots in the stator lamination for the first design approach (Design #1) since all of the rotor bridges are assumed to be nonmagnetic ($\mu = 1$). As a result, it is useful to introduce a Carter coefficient for the rotor to supplement that already introduced for the stator in order to model the effect of the nonmagnetic rotor bridges as an adjustment to the equivalent airgap length. This rotor Carter coefficient is calculated using the following equation, shown at the bottom of the page. where

Kcr is the rotor Carter coefficient
hm is the total thickness of the two magnets
rro is the rotor outer radius
g is the airgap thickness
p is the number of pole pairs.

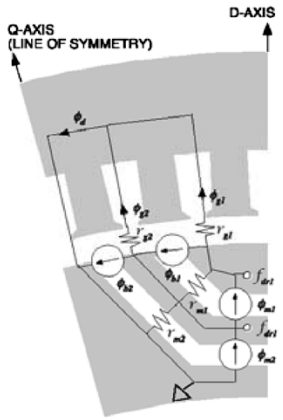

Fig. 4. Magnetic equivalent circuit for calculating magnet flux linkage $\lambda_{\rm PM}$ for baseline machine and Design #2.

It should be noted that this rotor-based Carter coefficient does not have to be introduced for Design #2 since only the rotor center posts are heat-treated to be nonmagnetic in this case. Finite element analysis has confirmed that the use of saturating bridges avoids the distinct rotor slotting effect that requires the use of a rotor Carter coefficient for Design #1.

C. Magnet Flux Linkage ($\lambda_{\rm PM}$) Calculation

Fig. 4 shows the equivalent circuit for calculating the magnet flux linkage $\lambda_{\rm PM}$ for the cases of regular M19 steel and Design #2 using saturable bridges. Here again, the key assumption for using this model is that the bridges are fully saturated so that they can be modeled as constant flux sources shorting fixed amount of the magnet flux linkage.

In the case of regular silicon steel:

$$\Phi_{b_1} = \Phi_{b_2} = B_s * (b_{rw} + c_{rw}) * L \tag{2}$$

where

Φ_{b1} and Φ_{b2} are flux linkage sources to model saturable bridges and center posts (baseline and Design #2)
B_s is the magnetic flux density saturation level of the rotor magnetic material (M19 or YEP-FA1)
b_{rw} is the bridge thickness
c_{rw} is half the center post thickness (for baseline case only; 0 for Design #2)
L is the active length.

For the Design #1 case with nonmagnetic bridges and center posts, the same model in Fig. 4 can be used except that the two flux linkage sources Φ_{b1} and Φ_{b2} are deleted since the saturable bridges and posts are both absent. As discussed above for the L_d calculations, the reluctances of the nonmagnetic bridges and

$$Kcr = \frac{\left(\frac{2*\pi*rro}{2*2*p}\right)}{\left(\frac{2*\pi*rro}{2*2*p}\right) - \left(\frac{2*hm}{\pi}\right) * \left(\tan^{-1}\left(\frac{hm}{2*g}\right) - \left(\frac{g}{hm}\right) * \ln\left(1 + \left(\frac{hm}{2*g}\right)^2\right)\right.} \tag{1}$$

TABLE II
TESTED CONDITIONS FOR ISG OPTIMIZATION

Test Points	Pass/Fail Tests
Initial Static calculations	Back-emf limit, 55 VDC Rational geometry
10 rpm	Motoring torque, 150 Nm Transient current density limit, 50A/mm^2
600 rpm	Generating power, 4000 W Steady-state current density limit, 20 A/mm^2
1500 rpm	Generating power, 3250 W Steady-state current density limit, 20 A/mm^2 Minimum machine efficiency, 80.3%
6000 rpm	Generating power, 6000 W Steady-state current density limit, 20 A/mm^2
Post-processing Calculations	Minimum system cost

center posts are sufficiently high that their impact on the magnet flux linkage can be ignored for Design #1. Similarly, the impact of the nonmagnetic center posts in Design #2 is very small so that they are not included in Fig. 4.

III. MACHINE DESIGN OPTIMIZATION RESULTS

After implementing the machine model modifications described in Section II, the IPM machine design optimization software was exercised using the same performance specifications and test conditions that were used for the existing starter/alternator [6], [9]. The key test conditions are summarized in Table II. The magnetic B-H curve and loss characteristics of the YEP-FA1 bi-state magnetic material were also added to the program, using data provided by the manufacturer [10]. However, this data is only needed for the rotor design since M19 steel was retained for the stator laminations for both Design #1 and #2 as discussed in Section II.

As noted in Section II, the machine design software incorporates a lumped-parameter thermal model for the IPM machine [8]. The availability of this thermal model makes it possible to directly set maximum temperature limits for the magnets and stator windings rather than setting maximum stator current limits as an indirect surrogate for these thermal limits. Temperatures were checked for all of the key machine components for each candidate design for every test condition in Table II. Any candidate design that causes these thermal limits (180 degC for stator windings and magnets) to be exceeded for any of the test conditions is eliminated from further consideration.

The machine design software was exercised leading to the identification of cost-optimized designs for both of the considered cases (Design #1 with nonmagnetic bridges and center posts, and Design #2 with nonmagnetic center posts only). The estimated drive system cost of the machine combined with its inverter is used as the optimization criterion [6], consistent with the approach used to develop the optimum baseline design with M19 steel in both the stator and rotor.

The fact that optimized designs emerged for both Design #1 and Design #2 is significant by itself since it indicates that the new material can be used in designs that meet all of the key performance criteria defined for the starter/alternator, including the test conditions listed in Table II. Stated differently, the software successfully identifies designs that minimize the impact of the poorer magnetic properties of the bi-state material in order to take advantage of its superior mechanical strength properties compared to conventional M19 steel.

TABLE III
COMPARISON OF MACHINE PARAMETERS FOR THE THREE DESIGNS

	Baseline S/A with M19 Stator and Rotor	Design #1: Non-magnetic Bridges and Center Posts	Design #2: Non-magnetic Center Posts
Number of Poles	*12*	*10*	*12*
Stator Material	*M19*	*M19*	*M19*
Rotor Material	*M19*	*YEP-FA1*	*YEP-FA1*
Magnet Remanent Flux Dens.	*0.28 [T]*	*0.15 [T]*	*0.215 [T]*
Bridge Thickness	*1 [mm]*	*4 [mm]*	*1 [mm]*
Center Post Thickness	*1 [mm]*	*1 [mm]*	*4 [mm]*
Stator Outer Diameter	271.7 [mm]	300 [mm]	271.7 [mm]
Active Length	60 [mm]	56.8 [mm]	60 [mm]
Total Length	90[mm]	100.1[mm]	90[mm]
Rotor Outer Radius	108.4 [mm]	116.2 [mm]	108.4 [mm]
Rotor Inner Radius	83.1 [mm]	87.2 [mm]	83.1 [mm]
Air Gap Length	0.635 [mm]	0.4 [mm]	0.635 [mm]
Effective Air Gap Thickness	0.696 [mm]	0.599 [mm]	0.696 [mm]
Air Gap Radius	109 [mm]	116.6 [mm]	109 [mm]
Active Rotor Volume	2215 [cm^3]	2411.6 [cm^3]	2215 [cm^3]
Winding Factor	0.9224	0.922	0.9224
Number of Series Turns	24	20	24
Number of Slots	72	60	72
Thickness of inner magnet	0.0029 [m]	0.0035 [m]	0.0029 [m]
Thickness of outer magnet	0.0057 [m]	0.0066 [m]	0.0057 [m]
Span of inner magnet	86.28[elect. Degrees]	80.3 [elect. Degrees]	86.28 [elect. Degrees]
Span of outer magnet	140.8 [elect. Degrees]	136.6 [elect. Degrees]	140.8 [elect. Degrees]

A. Optimized Machine Design Dimensions and Parameters

Table III provides a summary of the key dimensions and design parameters for the optimized IPM machines developed for Design #1 and Design #2 using the new bi-state magnetic material. A tabulation of the corresponding data for the baseline starter/alternator machine using all M19 steel is included in the table for convenient comparisons. Figs. 5–7 provide cross-sectional views of one pole for the baseline, Design #1, and Design #2 laminations, respectively.

A few observations are offered to help recognize the key physical differences between the three designs. First, it should be noted that Design #1 with nonmagnetic bridges and center posts optimized as a 10-pole configuration while the baseline and Design #2 machines both optimized with 12 poles. The impact of the new bi-state material is apparent first in the dimensions of the bridges and center posts in Design #1 and Design #2. While the baseline machine is limited to 1 mm bridge and post dimensions in order to avoid unacceptably high levels of magnet flux shunting, the bridge width in Design #1 and the center post width in Design #2 are both widened to 4 mm since they are nonmagnetic.

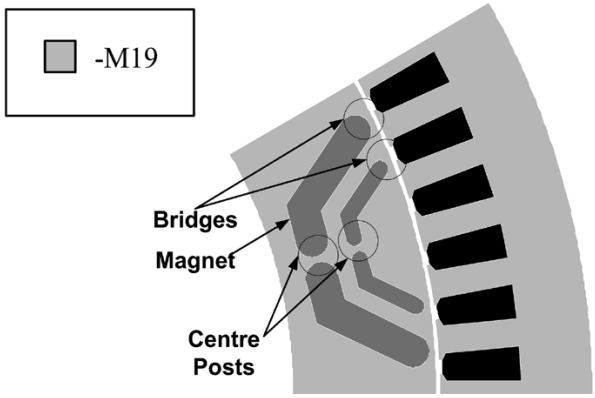

Fig. 5. Cross section of one pole of the baseline S/A with M19 stator and rotor.

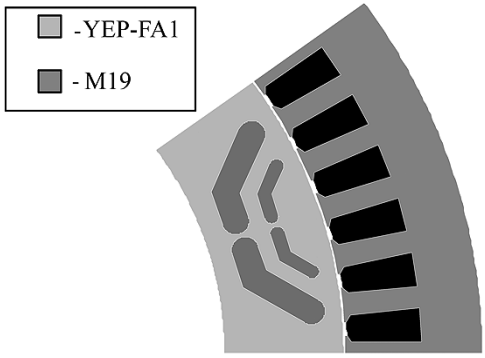

Fig. 6. Cross section of one pole of the Design #1 machine with nonmagnetic bridges and center posts.

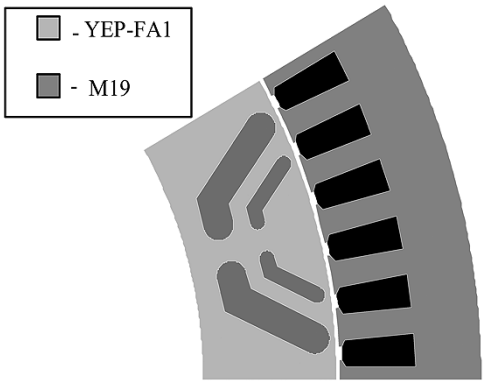

Fig. 7. Cross section of one pole of the Design #2 machine with nonmagnetic center posts only.

The impact of this flux shunting effect is most apparent in a comparison of the required magnet remanent flux density B_r for the three machines. It is interesting to note that the value of B_r is significantly lower for Design #1 (0.15 T) than for the baseline (0.28 T) and Design #2 (0.215 T) machines. An explanation for this difference can be found in the fact that only Design #1 has neither saturating bridges nor saturating center posts that shunt a fixed portion of the magnet flux, making it possible to use weaker magnets in this design.

This advantage for Design #1 is offset by other disadvantages. The outer stator diameter of the Design #1 machine (300 mm) is approximately 10% greater than that of either the baseline or Design #2 machines (271.7 mm). In addition, the airgap length

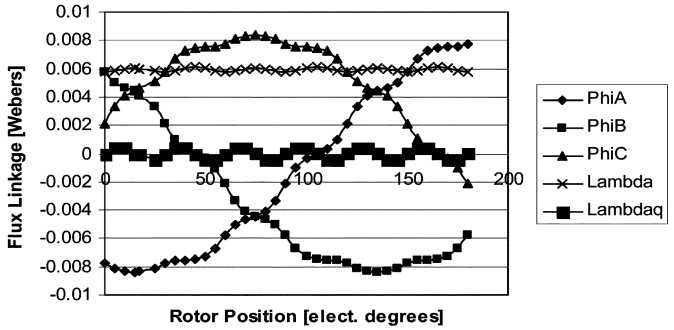

Fig. 8. Magnet flux linkage $\lambda_{\rm PM}$ using FEA (MagNet) for Design #1: nonmagnetic bridges and center posts.

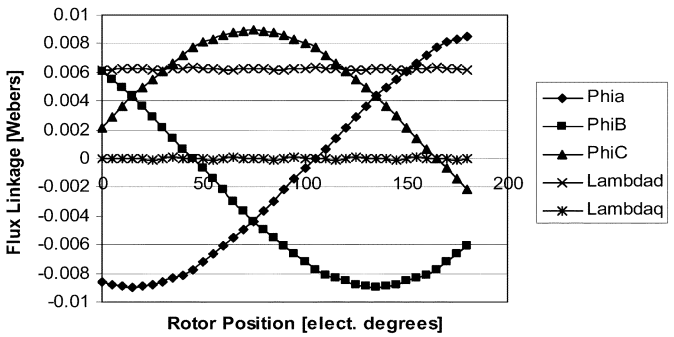

Fig. 9. Magnet flux linkage $\lambda_{\rm PM}$ using FEA (MagNet) for Design #2: nonmagnetic center posts only.

in the Design #1 machine (0.4 mm) is 37% shorter than the values for the baseline and Design #2 machines (0.635 mm). This smaller airgap compensates for the rotor slotting effect in Design #1 caused by the nonmagnetic bridges as described previously in Section II so that the effective airgaps for the three designs would be in the same vicinity. However, the smaller physical airgap makes the Design #1 machine more difficult to manufacture than the other two designs.

It will be shown in the following sections that the predicted performance of the Design #1 machine is inferior to that of Design #2. It is worth noting that if the same physical airgap length (0.635 mm) had been used in both designs, the performance of the Design #1 machine would be even poorer compared to Design #2 than that indicated in Table III with the adopted assumption.

B. Electromagnetic Finite Element Analysis Results

Electromagnetic finite element analysis (FEA) was used to confirm the machine parameters calculated using the lumped-parameters models and to calculate the torque ripple. The FEA software used for this analysis is MagNet 2D by Infolytica.

Figs. 8 and 9 show the FEA-predicted magnet flux linkage waveforms for phase A of the Design #1 and Design #2 machines, respectively, as a function of rotor position. The fundamental-frequency (rms) component of the magnet flux linkage $\lambda_{\rm PM1\,rms}$ for Design #1 (see Fig. 8) is 6 mWb-turns(rms) compared to 6.4 mWb-turns(rms) using the lumped-parameter model, corresponding to approximately 6% difference. This error is considered to be within an acceptable range based on

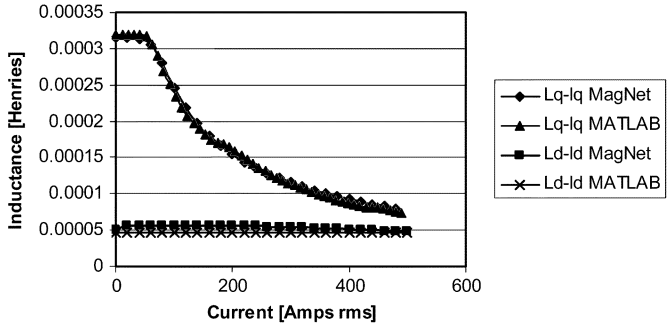

Fig. 10. L_q vs. I_q and L_d vs. I_d using lumped parameter model (MATLAB) and FEA (MagNet) for Design #1: nonmagnetic bridges and center posts.

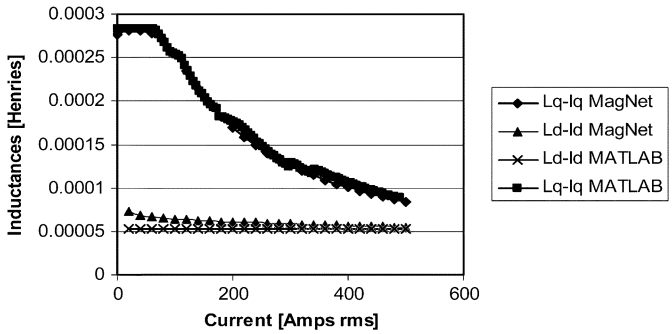

Fig. 11. L_q vs. I_q and L_d vs. I_d using lumped parameter model (MATLAB) and FEA (MagNet) for Design #2: nonmagnetic center posts only.

past experience with this IPM machine design process. For Design #2, the FEA-calculated magnet flux linkage (see Fig. 9) is 6.23 mWb-turns(rms) while the lumped-parameter models predicts 6.6 mWb-turns(rms), indicating a smaller difference of approx. 4%.

A comparison of the magnet flux linkage waveforms in Figs. 8 and 9 reveals that the waveform for the Design #1 machine contains significantly higher harmonic content than for the Design #2 machine. The underlying reason for this difference is that the slotting effect caused by the nonmagnetic bridges in the Design #1 machine results in considerably higher spatial flux harmonics in the airgap than the saturating bridges in Design #2. The impact of this difference will be discussed again below with regard to the torque ripple in the two machines.

Figs. 10 and 11 show the calculated L_q vs. I_q and L_d vs. I_d relationships for Design #1 and #2, respectively, using both the lumped-parameter model (MATLAB) and FEA (MagNet). It can be seen that there is good agreement between the FEA and lumped-parameter model predictions for L_q vs. I_q for both machines. There is also reasonably good agreement for the L_d vs. I_d curves except for low values of I_d for Design #2. The reason for this difference is the saturating bridges that are present in Design #2 but not Design #1, leading to conditions of incomplete saturation of the bridges under light-load conditions as discussed earlier in Section II-A.

Taken together, these FEA results build confidence in the validity of the predictions of the lumped-parameter model that includes the modifications in the rotor magnetic circuits required by the introduction of the nonmagnetic material in the bridge and center post regions.

TABLE IV
COMPARISON OF PERFORMANCE METRICS FOR THE THREE DESIGNS

	Baseline S/A with M19 Stator and Rotor	Design #1: Non-magnetic Bridges and Center Posts	Design #2: Non-magnetic Center Posts
Base Voltage	19.3 [Volts]	19.3 [Volts]	19.3 [Volts]
Stator Current [@ 150 N-m]	327 [Amps]	428 [Amps]	370 [Amps]
Pk-Pk Torque Ripple for Teavg = 150 N-m	< 10 %	~ 55 %	~ 24 %
Reduction in Rotor Peak Mechanical Stress	Baseline [330 MPa]	~ 50 %	~ 65 %
Mass of copper	*1.92 [Kg]*	*3.31[Kg]*	*1.92 [Kg]*
Mass of M19	*11.55 [Kg]*	*8.46 [Kg]*	*6.87 [Kg]*
Mass of YEP-FA1	*0 [Kg]*	*5.61 [Kg]*	*4.68 [Kg]*
Mass of magnets	*2.25 [Kg]*	*2.25 [Kg]*	*2.11 [Kg]*
Electromagnetic Weight	*15.6 [Kg]*	*19.6 [Kg]*	*15.9 [Kg]*
Estimated Copper Cost	$US 9.6	$US 16.6	$US 9.6
Estimated M19 Cost	$US 13.8	$US 8.5	$US 6.9
Estimated YEP-FA1 Cost	$US 0	$US 23.6	$US 20.4
Estimated Magnet Cost	$US 24.8	$US 24.8	$US 23.2
Estimated Machine Cost	$US 69	$US 114	$US 90
Estimated Converter Cost	$US 535	$US 569	$US 550
Estimated System Cost	$US 604	$US 683	$US 640
Phase Resistance	10.3 [mΩ]	5.4 [mΩ]	10.3 [mΩ]
Maximum back emf	23.9 [Vrms]	20 [Vrms]	24.98[Vrms]
PM flux linkage	6.3 [mWb]	6.4 [mWb]	6.6 [mWb]
Maximum rms switch current	231 [Arms]	302.8 [Arms]	262 [Arms]
Shear stress	4.9 [psi]	4.51 [psi]	4.91 [psi]

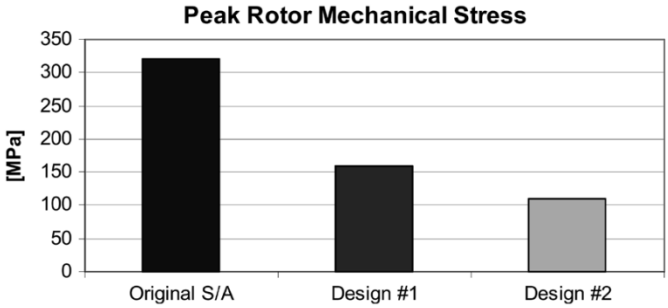

Fig. 12. Comparison of the peak rotor mechanical stress in the three designs.

C. Optimized Machine Metrics & Performance Comparisons

Table IV provides a summary of several key metrics and performance characteristics for the two new machine designs using the bi-state magnetic material as well as for the baseline all-M19 machine. An accompanying set of bar charts in Figs. 12 through 15 provides convenient visual comparisons of some of the key metrics including peak rotor mechanical stress, electromagnetic weight, machine cost, and drive system (motor plus converter) cost, respectively.

As indicated in Table IV and Fig. 12, both of the designs using the bi-state material achieve their primary objective of achieving a significant reduction in the peak rotor mechanical stress. Design #2 provides a stress reduction of approximately 65% com-

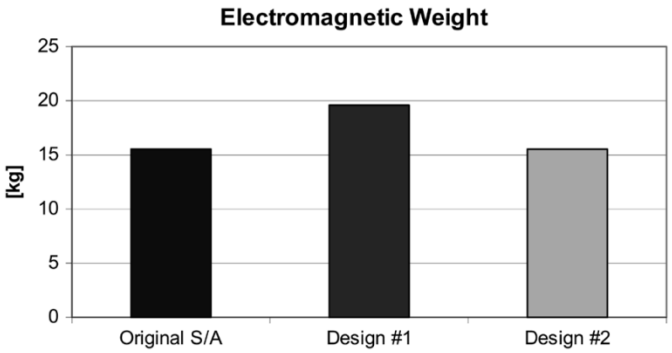

Fig. 13. Comparison of the electromagnetic weight of the three designs.

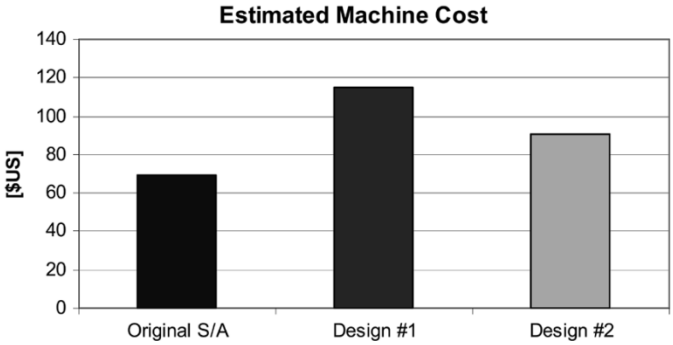

Fig. 14. Comparison of the estimated machine cost of the three designs.

pared to the baseline machine, while the corresponding stress reduction in Design #1 is in the vicinity of 50%. These stress reductions were calculated using the existing starter/alternator machine as the baseline because detailed structural finite element stress analyses using ANSYS were performed on this machine [5]. The results for the new machines are approximate since they are calculated using physics-based mechanical stress scaling rules discussed in [5] and [6].

These improvements must be weighed against notable disadvantages of using the new material that are apparent in the Table IV entries and accompanying bar charts. Consistent with earlier comments about its stator diameter, Design #1 results in a machine that is heavier than the baseline machine by approximately 26% (see Fig. 13), while the size and weight of the Design #2 machine are nearly identical to that of the baseline machine.

The estimated costs of the Design #1 and #2 machines are both significantly higher than that of the baseline machine (65% higher for Design #1 and 30% higher for Design #2; see Fig. 14). The principal cause of these differences is the cost of the bi-state YEP-FA1 material that is conservatively estimated to be three times the per-kilogram cost of M19 steel based on information received from the manufacturer. (A summary of the cost estimation formulas and material cost data for the machine and power converter are included in the Appendix, [6].)

The cost disadvantage associated with the new designs persists when comparing the projected combined cost of the machine and power converter (see Fig. 15, noting suppressed zero for cost axis). It is interesting to note that cost of the converter dominates the combined drive cost because of the high converter current ratings made necessary by the low dc bus voltage (42

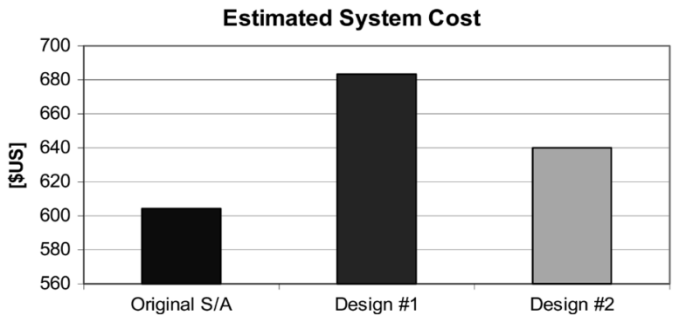

Fig. 15. Comparison of the estimated system cost of the three designs.

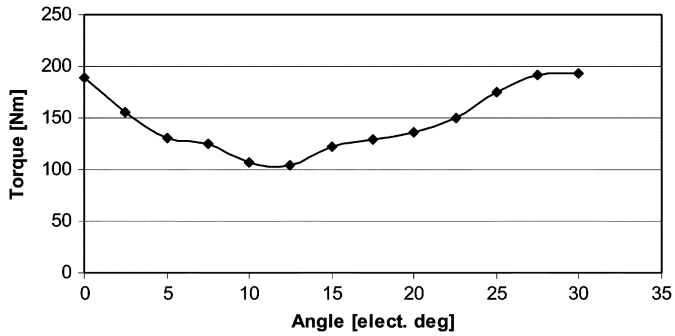

Fig. 16. Calculated torque ripple over one slot pitch (30° elec) for $I = 428$ Arms and $\gamma = 55°$ elec for Design #1: nonmagnetic bridges & center posts.

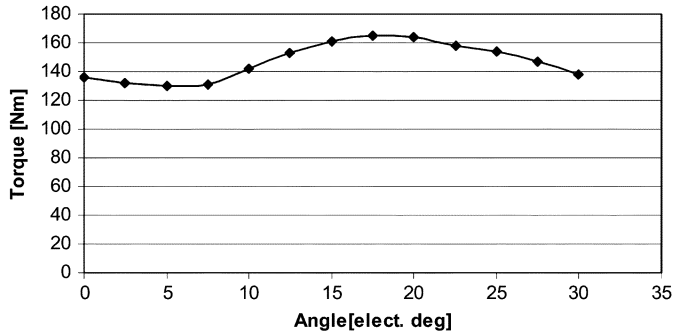

Fig. 17. Calculated torque ripple over one slot pitch (30° elec) for $I = 370$ Arms and $\gamma = 55°$ elec for Design #2: nonmagnetic center posts only.

Vdc). The cost of the converter for the Design #1 machine is estimated to be 6% higher than the baseline machine converter because of the significant increase in peak stator current (31%) it requires. The corresponding converter cost premium for the Design #2 machine is notably lower (3%), consistent with its smaller increase in stator current (13%).

Figs. 16 and 17 show the FEA-calculated torque ripple over one slot pitch with a control angle of 55 deg elec for Designs #1 and #2, respectively. For purposes of these analyses, neither the machine stator nor the rotor is skewed or provided with any special means for minimizing the torque ripple. The stator current is adjusted to the value required to deliver 150 N-m in each case. It can be seen that the torque ripple amplitude for Design #1 is more than twice the ripple amplitude for Design #2. Here again, the slotting effect caused by the nonmagnetic bridges in Design #1 appears very clearly in the torque ripple. In comparison, the saturating bridges in Design #2 play a useful role by attenuating the spatial flux harmonics in the airgap.

TABLE V
COMPARISON OF LOSSES, EFFICIENCY AND CALCULATED TEMPERATURES OF THE THREE MACHINES @ 600 rpm (4 kW GENERATING) FOR A COOLANT TEMPERATURE OF 70°C

	Baseline S/A with M19 Stator and Rotor	Design #1: Non-magnetic Bridges and Center Posts	Design #2: Non-magnetic Center Posts
	Losses[Watt] and Efficiency		
Armature losses	1539	1272	1663
Core losses	16	15.9	12.6
Rotor harmonic losses	42	43.7	28.6
Efficiency [%]	73	76.9	72
Component	**Temperatures [°C]**		
Frame	70.6	70.4	70.6
Stator yoke	86.8	85.7	88.1
Stator teeth	105.4	105	108.2
Coil side	133.1	129	138.2
End windings	168.7	151	176.6
Rotor surface	102.4	108	107.8
Inner magnet	102.4	108	107.8
Outer magnet	102.4	108	107.8
Bearings	70.9	71.1	71.25

Sensitivity analysis shows that the penalties in size, weight, and phase current suffered by the Design #1 and #2 machines are primarily caused by the lower magnetic flux density saturation level of the new bi-state material (1.3 T vs. 1.9 T for M19 silicon steel). Overall, the performance and metrics of the Design #2 machine are superior to those of the Design #1 machine in nearly all categories in Table IV.

D. Calculated Losses, Temperatures, and Efficiency

Table V provides a comparison of the calculated machine losses, efficiency, and internal temperatures for the three machines. It is interesting to note that the predicted efficiency of the Design #1 machine is nearly 4% higher than the baseline machine, while the efficiency of the Design #2 machine is 1% lower. The efficiency advantage of the Design #1 machine is due to its high copper mass compared to the baseline machine (72% higher) that causes the stator winding losses to drop by over 17% at the 600 rpm (4 kW generating) test condition.

The core losses listed in Table V include only loss contributions from the stator back iron and teeth. Magnet losses are low in these machines because the buried magnets see little flux variation and the use of ferrite magnets insures high resistivity, further reducing the magnet losses. Ferrite magnets are appealing for this automotive application because of their low cost. The system constraint on maximum back-emf forces all three of machine designs to low remanent flux densities, consistent with ferrite magnet properties.

The calculated internal machine temperatures for all three machines fall within safe maximum limits for the worst-case operating point, assuming a coolant temperature of 70 degC. The hottest temperature among all the entries is the end winding of Design #2 (177 degC) that approaches but does not exceed the maximum temperature limit. Although the loss characteristics of the YEP-FA1 material are somewhat poorer than those of M19 steel, the predicted rotor core losses are relatively low for all three machines. As a result, the calculated magnet temperatures all fall well within their safe operating ranges.

IV. CONCLUSION

This investigation has used a direct-drive automotive starter-alternator application to provide valuable insights into the strengths and limitations of applying a new bi-state soft magnetic material in IPM synchronous machines. This investigation has demonstrated that the new material can yield new machine designs that provide major improvements in the rotor structural integrity compared to the baseline all-silicon-steel starter-alternator machine while matching the size and weight of the baseline design.

However, the lower saturation flux density and permeability characteristics of the new bi-state material compared to conventional grades of silicon steel extract penalties that appear in one or more forms including higher stator current, higher losses, or larger/heavier machines. In addition, the expected cost premium for the new material pushes the total machine cost higher than that of an all-silicon-steel design.

Based on these observations, further work has been carried out to investigate whether the attractiveness of the new material for IPM machine applications can be enhanced by raising the maximum machine speed while holding the other performance requirements unchanged. Results of this extended investigation indicate that, by extending the high-speed limits of IPM machines [11], the bi-state magnetic material makes it possible to shrink the machine size—perhaps sufficiently to completely offset its cost premium.

The results of this ongoing work highlight the critical importance of finding the best-suited applications to optimally apply the advantages of this intriguing new material. In addition to the IPM synchronous machine and other applications previously cited [2]–[4], the bistate magnetic material may prove appealing in a variety of other machines and actuators that have moving elements needing "gaps" in their magnetic circuits. These include other types of ac synchronous reluctance machines (with or without magnets) and possibly even switched reluctance machines. Inevitably, tradeoffs between cost and performance will determine whether such solutions can eventually succeed in the marketplace.

APPENDIX
COST CALCULATION ALGORITHMS

The formula used to calculate the machine cost is as follows:

$$\text{Machine cost} = \sum_x (\text{Mass}_x * \text{Unit Cost}_x * \text{OverheadFactor}_x)$$

where the summation is taken over all of the materials used in the construction of the machine ($x = \text{copper}$, M19, magnet, and YEP-FA1 bi-state material, if used).

The formula used to calculate the converter cost is as follows:

$$\text{Converter cost} = \$423 + \left(\$0.4823 * \frac{I\max}{\sqrt{2}}\right) \qquad [\$US]$$

where $I\max$ is the maximum machine current, corresponding to machine starting current (150 N-m motoring) at 10 rpm.

TABLE A1
MATERIAL COST DATA

Material	Unit Cost	Overhead Factor
Copper	\$5/Kg	2
M19	\$1/Kg	2
YEP-FA1	\$3/Kg	2
Bonded Ferrite PM	\$11/Kg	1.1

ACKNOWLEDGMENT

The authors wish to thank S.-I. Yokoyama and M. Mita of Hitachi Metals Ltd., Japan, J. Kaneda of Hitachi Research Labs, Japan, and Dr. E.C. Lovelace of SatCon Technology Corp., Boston, MA, for their generous assistance in carrying out this study. The authors also gratefully acknowledge use of the facilities of the Wisconsin Electric Machines and Power Electronics Consortium (WEMPEC) during this investigation.

REFERENCES

[1] S. Yokoyama and T. Inui, "Magnetic properties of Fe-Cr-C and Fe-Cr-C-Ni alloys," *Tetsu-to-Hagane (Iron and Steel Institute of Japan)*, vol. 88, no. 4, 2002. (in Japanese).

[2] M. Mita, "Motor rotor with dual stage magnetic properties," in *Proc. 13th Ann. Symp. Incremental Motion Control Systems Devices*, Champaign, IL, Jul. 2001.

[3] M. Mita, N. Hirao, and F. Kimura, "A study of retainer ring made of 13.5Cr-0.6C-Fe dual state magnetic material," in *Proc. 15th IEEE Conf. Soft Magnetic Materials* , Bilbao, Spain, Sept. 2001.

[4] ——, "Magnetic screw rod using dual state 0.6C-13Cr-Fe bulk magnetic material," in *Proc. 46th Ann. Conf. Magnetism Magnetic Materials*, Seattle, WA, Nov. 2001.

[5] E. C. Lovelace, T. M. Jahns, T. A. Keim, and J. H. Lang, "Mechanical design considerations for conventionally-laminated ipm synchronous machine rotors," in *Proc. IEEE Int. Conf. Elec. Mach. Drives*, Cambridge, MA, Jun. 2001, pp. 163–169.

[6] E. C. Lovelace, "Optimization of a Magnetically Saturable Interior PM Synchronous Machine Drive," Ph.D. dissertation, Dept. Elect. Eng. Comp. Sci., Mass. Inst. Technol., Cambridge, MA, 2000.

[7] E. C. Lovelace, T. M. Jahns, and J. H. Lang, "A saturating lumped-parameter model for an interior PM synchronous machine," *IEEE Trans. Ind. Appl.*, vol. 38, no. 3, pp. 645–650, May/Jun. 2002.

[8] A. M. EL-Refaie, N. C. Harris, T. M. Jahns, and K. M. Rahman, "Thermal analysis of multi-barrier IPM synchronous machine using lumped parameter model," in *Proc. Int. Conf. Elec. Mach.*, Brugges, Belgium, Aug. 2002.

[9] E. C. Lovelace *et al.*, "Design and experimental verification of a direct-drive interior PM synchronous machine using a saturable lumped-parameter model," *Proc. Rec. IEEE Ind. Appl. Soc. Annu. Meeting*, pp. 2486–2492, Oct. 2002.

[10] Data sheet, "Properties of Composite Magnetic Material YEP-FA1," Metallurgical Res. Lab., Hitachi Metals Ltd., Data Sheet no. 020 113MG, Jan. 2002.

[11] A. M. EL-Refaie and T. M. Jahns, "Application of Bi-state magnetic material to automotive offset-coupled starter/alternatormachine," *IEEE Trans. Ind. Appl.*, vol. 40, no. 3, pp. 717–725, May/Jun. 2004.

Ayman M. EL-Refaie (S'95) received the B.Sc. and M.Sc. degrees in electrical power engineering from Cairo University, Cairo, Egypt, in 1995 and 1998, respectively. He received the M.Sc. degree in electrical engineering from the University of Wisconsin-Madison in 2002, where he is currently pursuing the Ph.D. degree in the Wisconsin Electric Machines and Power Electronics Consortium (WEMPEC) Group.

Currently, he is a Research Assistant at the University of Wisconsin–Madison. From 1995 to 1998, he was an Assistant Lecturer with Cairo University and the American University in Cairo. He participated in many projects involving the design of electrical power distribution systems. His interests include electrical machines and drives.

Thomas M. Jahns (S'73–M'79–SM'91–F'93) received the S.B. and S.M., and Ph.D. degrees in electrical engineering from the Massachusetts Institute of Technology, Cambridge, in 1974 and 1978.

Currently, he is Associate Director of the Wisconsin Electric Machines and Power Electronics Consortium (WEMPEC). In 1998, he joined the Department of Electrical and Computer Engineering, University of Wisconsin (UW)-Madison, as a Professor. Prior to joining UW-Madison, he was with GE Corporate Research and Development, Schenectady, NY, for 15 years, where he pursued new power electronics and motor drive technology in a variety of research and management positions. His research interests include permanent-magnet synchronous machines for a variety of applications ranging from high-performance machine tools to low-cost appliance drives. From 1996 to 1998, he conducted a research sabbatical at the Massachusetts Institute of Technology, where he directed research activities in the area of advanced automotive electrical systems and accessories as co-director of an industry-sponsored automotive consortium.

Dr. Jahns was awarded the William E. Newell Award by the IEEE Power Electronics Society (PELS) in 1999. He was recognized as a Distinguished Lecturer by the IEEE Industry Applications Society (IAS) in 1994–1995 and by IEEE-PELS in 1998–1999. He has served as President of PELS (1995–1996) and as a member of the IAS Executive Board from 1992–2001.